Atmos. Chem. Phys., 11, 11207–11220, 2011
www.atmos-chem-phys.net/11/11207/2011/
doi:10.5194/acp-11-11207-2011

Atmospheric Chemistry and Physics

Optimal estimation of tropospheric H_2O and δD with IASI/METOP

M. Schneider[1,2] **and F. Hase**[1]

[1]Karlsruhe Institute of Technology (KIT), IMK-ASF, Karlsruhe, Germany
[2]Agencia Estatal de Meteorología (AEMET), CIAI, Santa Cruz de Tenerife, Spain

Received: 2 May 2011 – Published in Atmos. Chem. Phys. Discuss.: 30 May 2011
Revised: 28 October 2011 – Accepted: 30 October 2011 – Published: 10 November 2011

Abstract. We present optimal estimates of tropospheric H_2O and δD derived from radiances measured by the instrument IASI (Infrared Atmospheric Sounding Interferometer) flown on EUMETSAT's polar orbiter METOP. We document that the IASI spectra allow for retrieving H_2O profiles between the surface and the upper troposphere as well as middle tropospheric δD values. A theoretical error estimation suggests a precision for H_2O of better than 35 % in the lower troposphere and of better than 15 % in the middle and upper troposphere, respectively, whereby surface emissivity and atmospheric temperature uncertainties are the leading error sources. For the middle tropospheric δD values we estimate a precision of 15–20 ‰ with the measurement noise being the dominating error source. The accuracy of the IASI products is estimated to about 20–10 % and 10 ‰ for lower to upper tropospheric H_2O and middle tropospheric δD, respectively. It is limited by systematic uncertainties in the applied spectroscopic parameters and the a priori atmospheric temperature profiles. We compare our IASI products to a large number of near coincident radiosonde in-situ and ground-based FTS (Fourier Transform Spectrometer) remote sensing measurements. The bias and the scatter between the different H_2O and δD data sets are consistent with the combined theoretical uncertainties of the involved measurement techniques.

1 Introduction

The continuous cycle of evaporation, vapour transport, cloud formation, and precipitation distributes water and energy around the globe. For reliable weather and climate predictions a thorough understanding of the atmospheric water cycle is indispensable. The complexity arises from the many different but competing processes that are involved. For instance, upper tropospheric humidity is controlled by various processes, e.g., by diffusion, by turbulent mixing, or by detrainment of water condensates inside convective clouds. For reliable climate prediction it is important to identify the relative contribution of the individual processes (upper tropospheric water vapour is a very effective greenhouse gas, Held and Soden, 2000). Water isotopologues offer promising opportunities for disentangling this complex situation. The ratio between different isotopologues (e.g., $HD^{16}O/H_2^{16}O$) is a proxy for evaporation sources, conditions at the condensation point, and the transport process experienced by the water mass. In the following we express $H_2^{16}O$ and $HD^{16}O$ as H_2O and HDO, respectively, and $HD^{16}O/H_2^{16}O$ as $\delta D = 1000\,‰ \times (\frac{[HD^{16}O]/[H_2^{16}O]}{SMOW} - 1)$, where $SMOW = 3.1152 \times 10^{-4}$ (SMOW: Standard Mean Ocean Water, Craig, 1961b).

The large potential of water isotopologues has been known since several decades. Already 50 years ago Craig (1961a) documented the strong correlation between the isotopologue ratios in precipitation and the atmospheric temperature. In the 1980s Joussaume et al. (1984) presented the first isotopologue incorporated Atmospheric General Circulation Model (AGCM). Since then such models have been used to interpret the isotopologue ratios in precipitation collected on the Earth's surface (e.g., Yoshimura et al., 2008). Today atmospheric water isotopologue research is still limited by the lack of lower to upper tropospheric data (in addition to the precipitation data collected on the Earth's surface). In the past tropospheric water isotopologue data have been obtained nearly exclusively during a few dedicated in-situ measurement campaigns (e.g., Ehhalt, 1974; Zahn, 2001; Webster and Heymsfield, 2003). However, what is needed is a consistent, long-term, high-quality, and area-wide observational data set.

Correspondence to: M. Schneider
(matthias.schneider@kit.edu)

Published by Copernicus Publications on behalf of the European Geosciences Union.

Only recently, there has been large progress in observing tropospheric water isotopologues by remote sensing techniques. Schneider et al. (2006b, 2010b) document the possibility of the global network of FTS (Fourier Transform Spectrometer) systems for a ground-based remote sensing of tropospheric H_2O and δD profiles. Worden et al. (2006), Frankenberg et al. (2009), and Yoshimura et al. (2011) show that the sensors TES (Tropospheric Emission Spectrometer) aboard AURA and SCIAMACHY (Scanning Imaging Absorption Spectrometer for Atmospheric Chartography) aboard ENVISAT allow for a space-based remote sensing of tropospheric H_2O and δD. The remote sensing techniques can provide continuous data sets and – if performed from space – they offer the possibility for almost global scale observations and thus novel research opportunities. For instance, Worden et al. (2007) used TES's isotopologue observation for documenting that rain recycling and evapotranspiration are important for the Amazonian water cycle. A good overview of the currently available tropospheric water isotopologue data sets obtained from different in-situ and remote sensing measurement techniques and their potential for atmospheric water cycle research is given by Risi et al. (2011a,b).

The space-based sensor IASI is, like TES, a Fourier transform spectrometer that measures thermal nadir spectra (a summary of IASI characteristics can be found for instance in Clerbaux et al., 2009). The potential of IASI for measuring tropospheric $H_2^{16}O$ and $HD^{16}O$ has been demonstrated by Herbin et al. (2009). Although IASI's spectral resolution is lower than TES's resolution (TES: $0.1\,cm^{-1}$; IASI: $0.5\,cm^{-1}$) it is very likely that IASI is able to detect tropospheric δD. IASI is very interesting for water cycle research, since it is flown aboard the operational meteorological satellite METOP and combines global coverage with high horizontal and temporal resolution: despite its small pixel size of 12 km diameter it covers almost the whole globe twice per day. Furthermore, IASI measurements will be guaranteed between 2006 and 2020 on a series of three METOP satellites.

In this paper we document that IASI can indeed detect tropospheric δD in addition to tropospheric H_2O. In Sect. 2 we present the applied retrieval method. Section 3 shows a theoretical estimate of the quality of our IASI H_2O and δD products and in Sect. 4 we empirically validate our IASI products. Therefore, we compare the IASI data to a large number of in-situ radiosonde measurements of H_2O as well as to ground-based FTS remote sensing measurements of H_2O and δD, which are made in coincidence to IASI overpasses.

2 The retrieval

2.1 The PROFFIT-nadir retrieval code

The thermal nadir retrieval code PROFFIT-nadir has been very recently developed as an extension to PROFFIT (PROFile Fit, Hase et al., 2004), which has been applied since many years by the ground-based FTS community for evaluating high resolution solar absorption spectra.

The code simulates the spectra and the Jacobians by the line-by-line radiative transfer model PRFFWD (PRoFit ForWarD model, Hase et al., 2004; Schneider and Hase, 2009a). It includes a ray tracing module (Hase and Höpfner, 1999) in order to precisely simulate how the radiation passes through the atmosphere. The vertical structure of the atmosphere is discretised and the amount of the absorber x at altitude level z can be described in form of a vector $\boldsymbol{x}(z)$. Similarly the frequency axis of the radiation spectrum is discretised and described by a vector $\boldsymbol{y}$ containing the radiances at the different spectral bins. PRFFWD accounts for the forward relation (F), that connects the spectrum ($\boldsymbol{y}$) to the vertical distribution of the absorbers ($\boldsymbol{x}$) and to parameters ($\boldsymbol{p}$) describing the state of the surface-atmosphere system as well as instrumental characteristics:

$$\boldsymbol{y} = \boldsymbol{F}(\boldsymbol{x}, \boldsymbol{p}) \tag{1}$$

The retrieval consists in adjusting the amount of the absorbers so that simulated and measured spectra agree. This is an under-determined problem, i.e., there are many different atmospheric states ($\boldsymbol{x}$) that produce almost identical spectra ($\boldsymbol{y}$). Consequently the problem requires some kind of regularisation. PROFFIT introduces the regularisation by means of a cost function:

$$[\boldsymbol{y} - \boldsymbol{F}(\boldsymbol{x}, \boldsymbol{p})]^T \mathbf{S}_\epsilon{}^{-1} [\boldsymbol{y} - \boldsymbol{F}(\boldsymbol{x}, \boldsymbol{p})] + [\boldsymbol{x} - \boldsymbol{x}_a]^T \mathbf{S_a}{}^{-1} [\boldsymbol{x} - \boldsymbol{x}_a] \tag{2}$$

Here the first term is a measure for the difference between the measured spectrum ($\boldsymbol{y}$) and the spectrum simulated for a given atmospheric state ($\boldsymbol{x}$), whereby the actual measurement noise level is considered ($\mathbf{S}_\epsilon$ is the noise covariance). The second term is the regularisation term. It constrains the atmospheric solution state ($\boldsymbol{x}$) towards an a priori state ($\boldsymbol{x_a}$), whereby the kind and the strength of the constraint are defined by the matrix $\mathbf{S_a}$. The constrained solution is reached at the minimum of the cost function Eq. (2).

Since the equations involved in atmospheric radiative transfer are non-linear, Eq. (2) is minimised iteratively by a Gauss-Newton method. The solution for the $(i+1)th$ iteration is:

$$\boldsymbol{x_{i+1}} = \boldsymbol{x_a} + \mathbf{S_a} \mathbf{K_i}^T (\mathbf{K_i} \mathbf{S_a} \mathbf{K_i}^T + \mathbf{S}_\epsilon)^{-1} [\boldsymbol{y} - \boldsymbol{F}(\boldsymbol{x_i}) + \mathbf{K_i}(\boldsymbol{x_i} - \boldsymbol{x_a})] \tag{3}$$

Whereby $\mathbf{K}$ is the Jacobian matrix which samples the derivatives $\partial y / \partial x$ (changes in the spectral fluxes $\boldsymbol{y}$ for changes in the vertical distribution of the absorber $\boldsymbol{x}$).

These regularisation and iteration methods are standard in the field of remote sensing. For more details please refer to the textbook of C. D. Rodgers (Rodgers, 2000).

In addition to these standard methods PROFFIT allows for a logarithmic scale retrieval. Therefore, the atmospheric

state vector, the a priori state and the a priori matrix, and the Jacobians have to be transferred on a logarithmic scale. This option is often called a positivity constraint since it assures positive solutions. It has proven to be very beneficial for tropospheric water vapour retrievals. The reason is that tropospheric water vapour concentrations are rather log-normally and not normally distributed, therefore the regularisation term of Eq. (2) is only adequately working on a log-scale (Schneider et al., 2006a).

The log-scale retrieval is also required for constraining ratios of absorbing species. Since $\ln\frac{[HDO]}{[H_2O]} = \ln[HDO] - \ln[H_2O]$ we can easily introduce an HDO/H_2O constraint in the regularisation term of Eq. 2 (we only have to fill in the respective elements of the matrix $\mathbf{S_a}$, Schneider et al., 2006b).

Furthermore, PRFFWD supports different spectroscopic line shape models, which is particularly important when retrieving water vapour profiles from very high resolution spectra (Schneider et al., 2011).

2.2 The IASI H_2O and δD retrieval

IASI records the thermal infrared emission of the Earth-atmosphere system between 645 and 2760 cm^{-1} with an apodised spectral resolution of 0.5 cm^{-1}. Figure 1 shows an IASI measurement, a simulation of this measurement, and the difference of both of the spectral window that we apply for our retrieval. The selected spectral window covers the region between 1190 and 1400 cm^{-1}. In this region there are strong lines of different water vapour isotopologues. Beside the main isotopologue $H_2^{16}O$, the secondary isotopologues $H_2^{18}O$, $H_2^{17}O$, and $HD^{16}O$ are important. In addition, there are significant spectroscopic features of CH_4 and N_2O and minor features of HNO_3, CO_2, and O_3 (a nice overview of the individual spectroscopic features in the selected spectral window is given in Herbin et al., 2009, Fig. 1). For the line-by-line simulations of these spectral signatures we apply the HITRAN 2008 spectroscopic line parameters (Rothman et al., 2009).

Except for O_3, whose weak signatures are only included in the forward calculation by assuming a climatological profile, all these species are simultaneously retrieved: while for CO_2 we scale a climatological profile, for CH_4, N_2O, and HNO_3 we apply a more relaxed ad hoc regularisation and allow for changes in the shape of a climatological profile. All these interfering species are retrieved on a linear scale.

The targeted water isotopologues are retrieved on a log-scale and regularised in an optimal estimation manner, in the sense that the a priori matrix $\mathbf{S_a}$ of Eq. (2) is deduced from the tropospheric water vapour covariances observed by radiosonde measurements: up to 12.5 km we use an a priori 1σ variability of 1.0 (on log scale!), between 12.5 and 25km it decreases linearly to 0.25, and for higher altitudes it remains constant at 0.25. The correlation lengths between the different altitude levels increase linearly from 2.5 km in the lower troposphere to 10 km in the stratosphere. On the log-scale we can use the same $\mathbf{S_a}$ for the different water isotopologues. We treat the $H_2^{16}O$, $H_2^{18}O$, and $H_2^{17}O$ isotopologues as a group and distinguish it from the $HD^{16}O$ isotopologue. This is justified since the fractionations between the oxygen isotopologues are typically one order of magnitude smaller than their fractionation with respect to the deuterium isotopologue. The applied H_2O log-scale a priori profile (x_a of Eq. 2) linearly decreases from the lower troposphere up to 15 km, whereby the slope of the decrease is deduced from the Tenerife radiosonde data sets (in Tenerife Vaisala radiosondes have been launched twice daily since many years about 15 km south of the location of the FTIR instrument). In the stratosphere we use a H_2O climatology obtained from MIPAS observations (J. J. Remedios, personal communication, 2007).

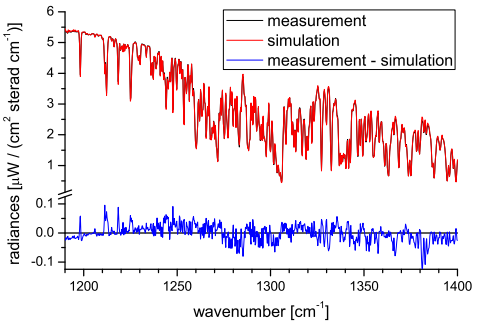

Fig. 1. Spectral region applied for the H_2O and δD retrieval. Black line: example of an IASI measurement; Red line: simulated IASI measurement; Blue line: residual (difference between measurement and simulation).

The HDO a priori profile is calculated from the H_2O profile using the $(\ln[HDO] - \ln[H_2O])$ climatology of Ehhalt (1974). From the Ehhalt (1974) measurements we also deduce the $(\ln[HDO] - \ln[H_2O])$ elements of the $\mathbf{S_a}$ matrix: an 1σ–$(\ln[HDO] - \ln[H_2O])$ variability of 80 ‰ and a correlation length between the different altitude levels which is identical to the one for $\ln[H_2O]$ (linear increase from 2.5 km in the lower troposphere to 10 km in the stratosphere).

In addition to the atmospheric species we retrieve the surface temperature and the atmospheric temperature profile. Both retrievals are constrained towards EUMETSAT's IASI level 2 temperatures. In the case of the atmospheric temperature retrieval the constraint is rather strong ($\mathbf{S_a}$ diagonal variances of 0.25^2 K^2). In this study we select observations over the ocean and thus use a constant surface emissivity of 1.0.

Concerning cloud detection we rely on EUMETSAT's IASI level 2 cloud product. We only evaluate pixel that are measured for cloud free conditions, whereby we define as cloud free if EUMETSAT's level 2 fractional cloud cover parameter is below 15 %. For more details about EUMETSAT's

level 2 cloud products please refer to the EUMETSAT IASI level 2 product guide (2011).

In this study we only work with IASI morning overpasses.

2.3 The difference to Herbin et al. (2009)

Herbin et al. (2009) show that tropospheric HDO in addition to H_2O can be optimally estimated from IASI spectra. They retrieve the H_2O and HDO profiles independently and a posteriori calculate the HDO/H_2O ratios. However, the retrieved H_2O and HDO profiles suffer from different vertical sensitivity (compare the averaging kernels of Figs. 4 and 5 of Herbin et al., 2009). Therefore, the H_2O and HDO profiles are not directly comparable (see also Rodgers, 2000; Rodgers and Connor, 2003). The a posteriori calculation of HDO/H_2O ratios from independently retrieved H_2O and HDO profiles leads to large errors, especially in the troposphere where even minor changes in the kernels significantly affect the retrieved H_2O and HDO profiles: in the troposphere the H_2O and HDO mixing ratios change over several orders of magnitudes and large changes often take place over rather small vertical distances. Moreover, when performing an independent retrieval of H_2O and HDO it is difficult to establish a reasonable HDO/H_2O sensitivity estimation.

In contrast to Herbin et al. (2009) we perform an optimal estimation of H_2O, HDO, and in addition of HDO/H_2O, i.e. we make use of the HDO/H_2O a priori knowledge. Thereby our HDO/H_2O result is not affected by different HDO and H_2O sensitivities. Our retrieval produces the best HDO/H_2O estimate for the given measurement and we can easily document the sensitivity of the remote sensing system with respect to HDO/H_2O. The constraint with respect to the HDO/H_2O ratio becomes possible by transferring the whole inversion problem on a logarithmic scale. Then $\ln([\mathrm{HDO}]/[\mathrm{H_2O}]) = \ln[\mathrm{HDO}] - \ln[\mathrm{H_2O}]$ and we can easily introduce the HDO/H_2O constraint by an adequate occupation of the Sa matrix (a priori covariance matrix) that connect the HDO and H_2O states. For further details please refer to Schneider et al. (2006b).

Moreover, using a logarithmic scale is equivalent to assuming a log-normal a priori probability density function (pdf), which better represents the true pdf of H_2O and HDO than a Gaussian a priori pdf (Gaussian a priori pdf is implicitly assumed when using a linear scale like Herbin et al., 2009). This has already been demonstrated by Schneider et al. (2006a).

3 Product characterisation

3.1 Vertical resolution and sensitivity

An important addendum of the retrieved solution vector is the averaging kernel matrix **A**. It samples the derivatives $\partial\hat{x}/\partial x$ (changes in the retrieved concentration $\hat{x}$ for changes in the actual atmospheric concentration x describing the smoothing

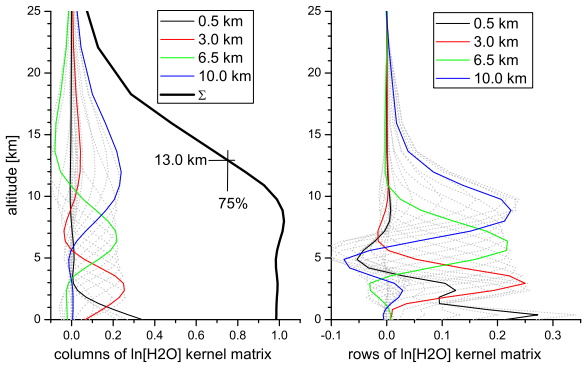

Fig. 2. Averaging kernel matrix for $\ln[H_2O]$. Left panel: column kernels; Right panel: row kernels. Grey dotted lines: for all atmospheric model grid levels; Black, red, green, and blue lines: for the 0.5, 3, 6.5, and 10 km grid level, respectively; Thick black line in the left panel: Sensitivity (sum of the column kernels).

of the real atmospheric state by the remote sensing measurement process:

$$(\hat{\boldsymbol{x}} - \boldsymbol{x_a}) = \mathbf{A}(\boldsymbol{x} - \boldsymbol{x_a}) \tag{4}$$

In addition, the trace of **A** quantifies the amount of information introduced by the measurement. It can be interpreted in terms of degrees of freedom (DOF) of the measurement.

Concerning differences in $\ln[H_2O]$ and $(\ln[\mathrm{HDO}] - \ln[H_2O])$ we can write:

$$\Delta(\ln[\mathrm{H_2O}]) \approx \frac{\Delta[\mathrm{H_2O}]}{[\mathrm{H_2O}]} \tag{5}$$

and

$$\Delta(\ln[\mathrm{HDO}] - \ln[\mathrm{H_2O}]) \approx \frac{\Delta\left(\frac{[\mathrm{HDO}]}{[\mathrm{H_2O}]}\right)}{\frac{[\mathrm{HDO}]}{[\mathrm{H_2O}]}} = \frac{\Delta\left(\frac{[\mathrm{HDO}]}{[\mathrm{H_2O}]}\right) + \frac{[\mathrm{HDO}]}{[\mathrm{H_2O}]}}{\frac{[\mathrm{HDO}]}{[\mathrm{H_2O}]}} - 1 \tag{6}$$

Therefore, in the following we will use differences in $\ln[H_2O]$ interchangeably with relative differences in $[H_2O]$ and differences in $(\ln[\mathrm{HDO}] - \ln[H_2O])$ with differences in δD.

Figure 2 shows the averaging kernels for a typical IASI H_2O retrieval over the ocean (surface temperature 290 K) and for cloud free conditions. The left panel depicts the column kernels. They describe the response of the retrieved state vector on a 1.0 disturbance of the real state vector. We can observe that the maxima of these response functions generally peak at the altitude of the disturbances: the black line describes the response for an 1.0 disturbance at 0.5 km and it peaks close to 0.5 km, the red line represents the response on a disturbance at 3 km and it peaks close to 3 km, etc. The

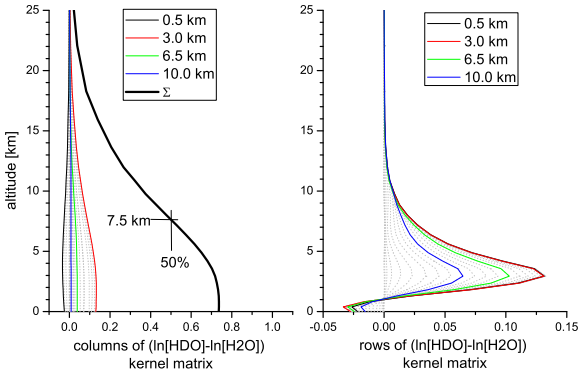

Fig. 3. Same as Fig. 2 but for $\ln[\mathrm{HDO}] - \ln[\mathrm{H_2O}]$.

FWHM (full width at half maximum) of these kernels can be interpreted as the vertical resolution of the remote sensing measurement. We find FWHMs of about 2.5, 4.5, and 9 km for the lower, middle, and upper troposphere, respectively. The sum of the column kernels (depicted as thick black line) indicates the overall sensitivity of the retrieved state with respect to the real state. IASI is well sensitive with respect to atmospheric H_2O from the surface up to 13 km (sensitivity better than 75 %). For the cloud free H_2O retrievals we find a typical DOF value of 3.4.

The right panel of Fig. 2 shows the rows of the averaging kernel matrix. They indicate the altitude regions that mainly contribute to the retrieved state. We see that the state retrieved at different altitudes, e.g., 0.5, 3, 6.5, and 10 km, reflects well the real state at these altitudes.

Figure 3 depicts the same as Fig. 2 but for δD. In contrast to H_2O our IASI δD retrieval can not resolve profiles of δD. Only in the lower troposphere the sensitivity (sum of column kernels) is close to 75 %. Above 3 km it starts to decrease steadily. At 7.5 km it is 50 %. The DOF value is typically between 0.6 and 0.8. The right panel documents that the δD values retrieved at different altitude levels mainly reflect the real δD state between 2 and 5.5 km. Over the ocean and under cloud free conditions we can only detect δD variation in this altitude range. Our IASI δD sensitivity estimate is similar to the one obtained by Worden et al. (2006) for TES.

3.2 Propagation of uncertainty sources

We consider three groups of uncertainty sources: (1) uncertainty in the thermal radiation emitted by the Earth-atmosphere system, (2) uncertainty in the spectroscopic line parameter of the water isotopologues, (3) uncertainty due to spectroscopic features of interfering species, and (4) measurement noise. The propagation of these uncertainties can be calculated by (e.g., Rodgers, 2000):

$$\delta \boldsymbol{x} = \mathbf{G}\mathbf{K_p}\boldsymbol{\epsilon_p} \quad (7)$$

Whereby $\mathbf{G} = (\mathbf{K}^T {\mathbf{S}_\epsilon}^{-1}\mathbf{K} + {\mathbf{S}_\mathbf{a}}^{-1})^{-1}\mathbf{K}^T {\mathbf{S}_\epsilon}^{-1}$ is the gain matrix, which samples the derivatives $\partial\hat{x}/\partial y$ (changes in the retrieved state $\hat{x}$ for changes at the spectral bin y), $\mathbf{K_p}$ is the parameter Jacobian, which samples the derivatives $\partial y/\partial p$ (changes at the spectral bin y for changes in the parameter p), and $\boldsymbol{\epsilon_p}$ is a vector describing the uncertainty of parameter p.

The error patterns $\delta\boldsymbol{x}$ give an extensive overview of the errors' importance and characteristics, including the correlation and anti-correlation of the error between different altitudes. In this context they contain more information than the often used square root values of the diagonal of an error covariance matrix $\delta\mathbf{S} = \mathbf{G}\mathbf{K_p}\boldsymbol{\epsilon_p}(\mathbf{G}\mathbf{K_p}\boldsymbol{\epsilon_p})^T$. For readers not interested in these details the altitude dependent correlation and anti-correlation of the errors can easily be removed by calculating the absolute values of the error patterns.

3.2.1 Thermal radiation

IASI measures the thermal radiation emitted by the Earth-atmosphere system. The intensity and broadband characteristic of this radiation depends on the emissivity and temperature of the Earth's surface and on the atmospheric vertical temperature profile. Thus the emissivity and temperatures importantly affect the interpretation of an IASI measurement. For the surface emissivity we assume an uncertainty of +5 % (we calculate how a by 5 % too large emissivity would affect the retrieved H_2O profile). Although this work is limited to ocean scenes, for which emissivity is rather well known and close to 1.0, we include an emissivity error estimation thinking in our land scene retrievals planed in the near future. For the surface and atmospheric temperatures we assume uncertainties of +1 K, whereby we distinguish between the different layers: surface–2 km, 2–5 km, and the whole atmosphere above 5 km.

The leftmost panel of Fig. 4 documents how these uncertainties propagate into the retrieved H_2O profiles. An erroneously too large emissivity will lead to a significant underestimation of boundary layer H_2O. It will be an important error source for land scene retrievals. Uncertainties in the surface temperature are effectively identified by the surface temperature retrieval and do not significantly affect the retrieved H_2O profiles. This is in contrast to uncertainties in atmospheric temperatures which strongly interfere with the retrieved H_2O: if the assumed atmospheric temperature is by 1 K too large the retrieval overestimates the H_2O amounts by up to 15 %.

Figure 5 shows the respective δD error patterns. It documents that for δD atmospheric temperature errors above 2 km are dominating this group of uncertainty sources.

3.2.2 Spectroscopic parameters

The line-by-line modelling relies on the parameters collected in spectroscopic databases like HITRAN (Rothman et al., 2009). For our estimation we consider the line parameter

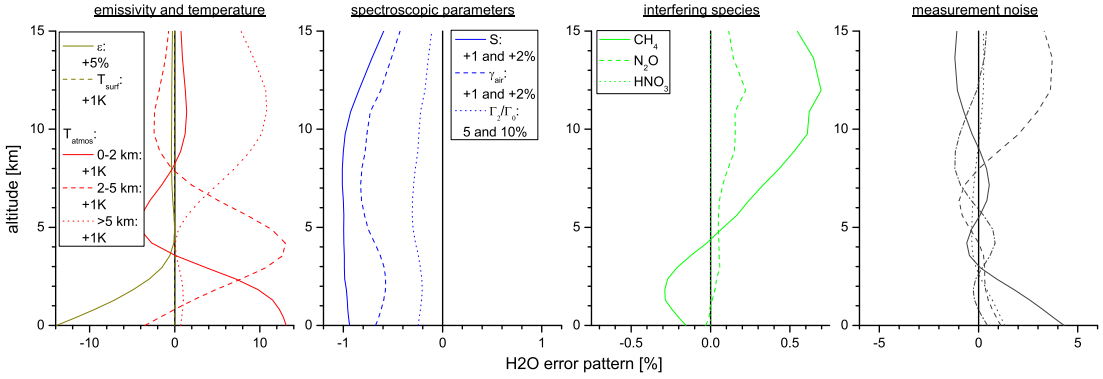

Fig. 4. H_2O error patterns from the left to the right for different groups of uncertainty sources: emissivity (ϵ) and temperature, spectroscopic line parameters (S, γ_{air}, and Γ_2/Γ_0), interfering absorber (CH_4, N_2O, and HNO_3), and measurement noise, respectively.

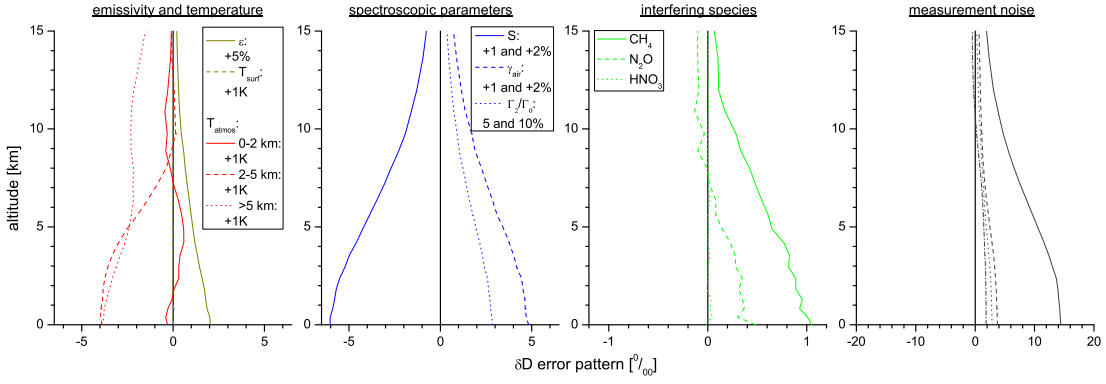

Fig. 5. Same as Fig. 4 but for δD.

Table 1. Statistics of DOFs for cloud free IASI retrievals over the subtropical northern Atlantic (number of observations: 72).

product	mean of DOF	std of DOF
H_2O	3.43	0.25
δD	0.68	0.14

Table 2. Assumed spectroscopic parameter uncertainty for H_2O and HDO.

source	H_2O	HDO
line strength, S	+1 %	+2 %
pres. broad. coef., γ_{air}	+1 %	+2 %
SDV strength, Γ_2/Γ_0	+5 %	+10 %

uncertainty as collected in Table 2: the line strength (S), the air pressure broadening coefficient (γ_{air}), and the applied line shape model (strength of speed-dependence: Γ_2/Γ_0, D'Eu et al., 2002). In Schneider et al. (2011) it has been documented that the application of different line shape models strongly affect the H_2O profiles estimated from very high resolution spectra.

We assume different errors for the H_2O and HDO isotopologues in order to estimate how an inconsistency between the H_2O and HDO line parameters affects the δD retrievals.

The line strength parameter dominates the spectroscopic parameter uncertainty (see second panel form the left of Fig. 4). For thermal nadir sounding with a spectral resolution of $0.5\,\text{cm}^{-1}$ the line shape is of secondary importance. In ground-based solar absorption remote sensing applying very high resolution spectra it is vice versa: line shape uncertainties dominate line strength uncertainties (Schneider et al., 2010c).

For δD the spectroscopic line parameter uncertainties are of similar importance than the emissivity and temperature uncertainties (compare first and second panel from the left of Fig. 5). This is in contrast to H_2O, where the errors due spectroscopic line parameter uncertainties are much smaller than the errors due to emissivity and temperature uncertainties.

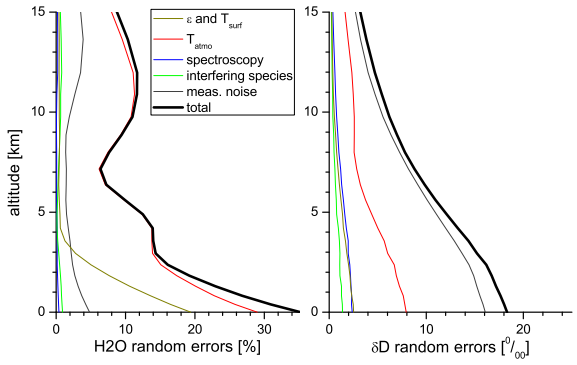

Fig. 6. Random error budgets: left panel for H_2O and right panel for δD.

The reason for the relatively low importance of emissivity and temperature uncertainties in the case of δD is that these uncertainties propagate similarly into H_2O and HDO and widely cancel out when calculating the ratio, whereas inconsistency in the H_2O and HDO line parameters do not cancel out (Schneider et al., 2006b).

3.2.3 Interfering species

In the analysed spectral window there are also important spectral signatures of CH_4, N_2O, and HNO_3. These signatures might interfere with the signatures of the water isotopologues and thus affect the retrieved H_2O and δD. In order to assess the importance of this interference we increase the line strength (S) and the pressure broadening parameters (γ_{air}) of these species by 2 % and observe the impact on the H_2O and δD retrievals. Changing S and γ_{air} has a similar effect on the spectra as changing the total column amount and the vertical distribution of the absorber.

The third panel from the left of Figs. 4 and 5 document that CH_4 is the most important interfering species. The interfering errors of N_2O are rather small and the ones of HNO_3 can be completely neglected. Concerning H_2O the upper tropospheric CH_4 interfering errors are almost as important as respective errors due to uncertainties in the spectroscopic parameters of H_2O.

3.2.4 Measurement noise

Naturally, noise in the measured spectra will lead to random errors in the retrieved products. When calculating the propagation of the measurement noise we can substitute $\mathbf{K_p}\boldsymbol{\epsilon}_p$ in Eq. (7) by the vector $\boldsymbol{\epsilon}_y$ representing the noise at each spectral bin. For our simulation we assume for each element of $\boldsymbol{\epsilon}_y$ a value of 2×10^{-2} µW/(cm^2 sr cm^{-1}), which is an IASI radiometric noise value that has been established from a set of representative spectra (Clerbaux et al., 2009, Fig. 2). The four leading error noise patterns are depicted in the rightmost panel of Figs. 4 and 5.

For H_2O we observe largest errors in the lower and upper troposphere, whereby the sign of these errors is partly anti-correlated, i.e., large positive errors in the lower troposphere often come along with negative errors in the upper troposphere (see error pattern represented by the solid grey line). In the middle troposphere measurement noise seems to be less important than in the lower and upper troposphere.

For δD the measurement noise error patterns have no significant vertical structure, i.e., they are of the same sign at all altitude levels.

3.2.5 Error budget

The uncertainties of surface temperature and emissivity, atmospheric temperatures, concentration profiles of interfering species, and the measurement noise contribute to the overall random error budget. The random error of each group can be calculated as the root-square-sum of the individual contributions, e.g., the atmospheric temperature random error is the root-square-sum of the atmospheric temperature error patterns as depicted in the leftmost panels of Figs. 4 and 5: $\sqrt{T^2_{0-2\text{km}} + T^2_{2-5\text{km}} + T^2_{>5\text{km}}}$. In addition $\mathbf{G}$ and $\mathbf{K_p}$ of Eq. (7) slightly depend on the surface conditions, atmospheric conditions, and on IASI's observation geometry, i.e., the patterns of Figs. 4 and 5 slightly vary from observation to observation. This additional random error contribution is considered in the budgets presented in Fig. 6 and it is the reason why even a systematic uncertainty source, like the uncertainties in the spectroscopic line parameters of H_2O and HDO produce a random error component (see blue curves in Fig. 6).

Concerning H_2O the total random error (thick black line) is dominated by the uncertainties in the atmospheric temperature (red line). Furthermore, in the lower troposphere and for future land scene retrievals uncertainties in surface emissivity (dark yellow line) will become important. In the upper troposphere measurement noise (dark grey line) can make a significant contribution to the total random error.

We estimate a IASI δD precision of about 18 ‰. It is clearly controlled by the measurement noise, which is the leading random error (see dark grey line in the right panel of Fig. 6). The reason is that most other errors propagate similarly into H_2O and HDO and thus cancel out in the H_2O/HDO ratio.

These estimations document, that IASI's low noise level is decisive for its δD remote sensing capability: tropospheric δD variations are typically 80 ‰. If IASI's noise level was four times higher the total δD random error would be close to 80 ‰ and a single IASI measurement pixel would hardly reach the precision level required for the observation of tropospheric δD.

The systematic uncertainties in the spectroscopic line parameters produce systematic errors in the IASI H_2O and δD data. Furthermore, there might be a systematic uncertainty in the applied a priori atmospheric temperature profile (EU-

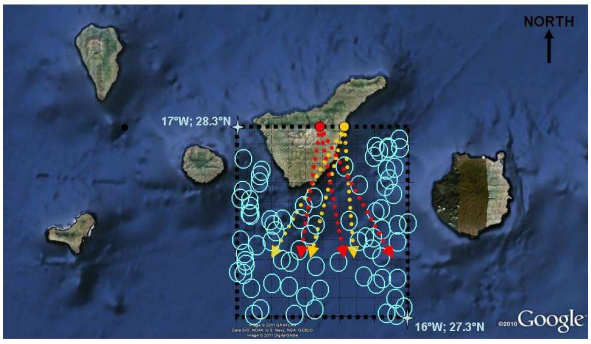

Fig. 7. The area south of the Island of Tenerife that is used for our validation exercise. The cyan circles depict the individual IASI measurement pixels used in the study. The red arrows indicate the airmass detected by Izaña's ground-based FTS system and the yellow arrows the airmass detected by the Viasala RS92 during the IASI morning overpasses.

METSAT's IASI level 2 temperatures). Assuming systematic temperature uncertainties of below 0.5 K and spectroscopic line parameter uncertainties as listed in Table 2 we estimate a total systematic error in the lower to upper tropospheric H_2O data of about 20–10 % and in the middle tropospheric δD data of about 10 ‰ (see error patterns of Figs. 4 and 5).

4 Product validation

The scientific value of this new IASI observational data strongly depends on the documentation of its quality. While there are H_2O data available from various techniques that can serve as a validation reference (e.g., meteorological radiosondes) there is currently only one technique that can measure δD at different tropospheric altitudes and on a regular basis: the ground-based FTS technique (Schneider et al., 2010b). In this section we show a comparison of our IASI products to data from Vaisala radiosondes and from a ground-based FTS system.

4.1 The validation site

Figure 7 shows a map of the western part of the Canary archipelago situated in the northern subtropical Atlantic Ocean about 300 km west of the African west coast at about 28° N. The center of the map shows Tenerife, the main Island of the Western Canary province. It hosts the Izaña Atmospheric Research Centre (IARC, www.aemet.izana.org, indicated as red dot in the centre of Tenerife). IARC is run by the Meteorological State Agency of Spain (AEMET) and has been contributing since many years with high-quality atmospheric observations to a variety of international atmospheric monitoring networks. Since 1999 high resolution infrared solar absorption spectra have been recorded by a ground-based FTS system. The high quality of the tropospheric H_2O and δD measured at Izaña has been demonstrated in several studies (e.g., Schneider et al., 2010a,b). About 20 km east of the observatory on the coastline there is a launch pad for meteorological radiosondes (indicated as yellow dot in Fig. 7). There Vaisala RS92 radiosondes are launched twice per day at 00:00 and 12:00 UT. The red and yellow arrows denote the airmass that is typically analysed during the IASI morning overpasses by the FTS system and the radiosonde, respectively. The cyan circles mark IASI cloud free pixels (12 km diameter) that fall within the selected validation box between 27.3 and 28.3° N and 17.0 and 16.0° W (indicated by the black dotted lines) and that have been measured between March and June 2009 within 60 min of an RS92 or FTS observation. Table 3 shows the number of measurements that have been used for this validation exercise.

Table 3. Number of individual IASI pixel measurements, Vaisala RS92 radiosondes, and ground-based FTS measurements used for the validation exercise.

Instrument	Number of measurements
IASI	72
RS92	27
FTS	66

4.2 Comparison to meteorological radiosondes Vaisala RS92

We correct the radiosonde humidity data by the formulas given in Vömel et al. (2007). Furthermore, we adjust the vertically highly-resolved Vaisala RS92 profile ($\boldsymbol{x}_{\mathrm{RS92}}$) to the limited vertical resolution of the IASI profiles. Therefore, we convolve $\boldsymbol{x}_{\mathrm{RS92}}$ with the averaging kernels. According to Eq. (4) it is:

$$\hat{\boldsymbol{x}}_{\mathrm{RS92}} = \mathbf{A}(\boldsymbol{x}_{\mathrm{RS92}} - \boldsymbol{x}_a) + \boldsymbol{x}_a \tag{8}$$

The result is an RS92 profile ($\hat{\boldsymbol{x}}_{\mathrm{RS92}}$) with the same vertical resolution and sensitivity as the IASI profile.

The left panels of Fig. 8 show correlations between the H_2O concentrations obtained by the RS92 and IASI at different altitudes. With the exception of the boundary layer, the correlation coefficients are about 0.8 or higher. Please note that all the correlation coefficients are written inside the respective plots. In particularly good is the correlation in the upper troposphere at 10 km (correlation coefficient of 0.94).

The second column of Table 4 informs about the relative differences between RS92 data and our PROFFIT IASI H_2O products. It collects the bias and the scatter (mean and 1σ standard deviation of the difference) between both data sets for the altitudes shown in Fig. 8: for 0.5, 3.0, 6.5, and 10.0 km, in representation of the boundary layer, the lower,

Table 4. Relative differences (bias and scatter) between our IASI PROFFIT, EUMETSAT's IASI, and the coincident RS92 H_2O data sets (mean $\pm$ std of $2 \times \frac{X-Y}{X+Y}$) [%].

altitude region	$IASI_{PRF} - RS92$	$IASI_{EUM} - RS92$	$IASI_{PRF} - IASI_{EUM}$
BL (0.5 km)	-0.9 ± 26.2	-11.9 ± 30.1	$+11.0 \pm 21.8$
LT (3.0 km)	$+3.4 \pm 27.2$	-0.2 ± 29.2	$+3.6 \pm 9.9$
MT (6.5 km)	-5.4 ± 35.2	-3.5 ± 36.6	-2.0 ± 6.7
UT (10.0 km)	-5.6 ± 22.8	$+11.2 \pm 23.1$	-16.7 ± 6.0

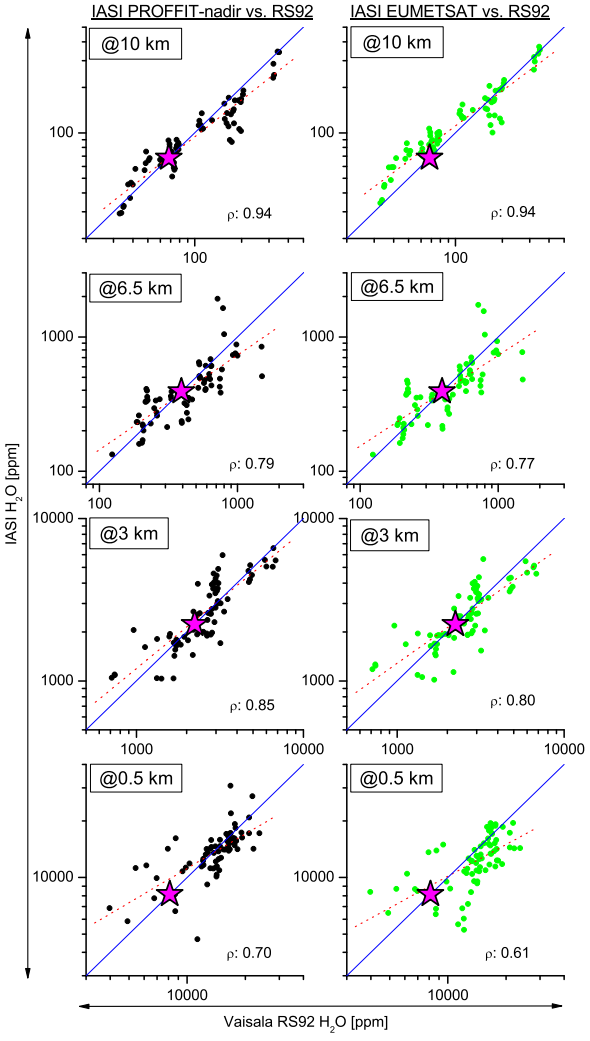

Fig. 8. Correlation plots between IASI and Vaisala RS92 H_2O data. From the bottom to the top for 0.5, 3, 6.5, and 10 km altitude. Left panels for IASI PROFFIT-nadir and right panels for IASI EUMETSAT products. The magenta stars, the red dotted line, and the blue solid line, indicate the applied a priori values, the linear regression line, and the diagonal ($x = y$) line, respectively.

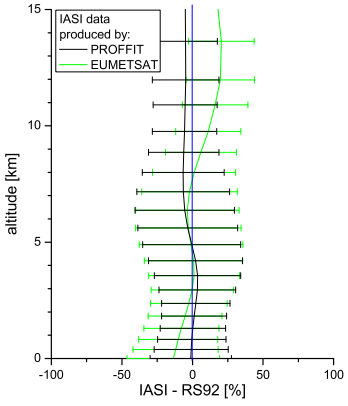

Fig. 9. Statistics of difference between IASI and Vaisla RS92 H_2O profiles. Black line for IASI PROFFIT-nadir and green line for IASI EUMETSAT profiles, respectively.

middle, and upper troposphere (BL, LT, MT, and UT), respectively. We observe no significant bias. It lies almost within ± 5 % throughout the troposphere. This indicates that there are no significant systematic errors in the applied EUMETSAT IASI level 2 temperatures profiles, since such temperature errors would produce a strong bias in our IASI H_2O profiles (see left panel of Fig. 4). The scatter between the two data sets is mostly lower than 35 %. Except for the boundary value the observed scatter is larger than the theoretically estimated random error of about 15 %. We think that the increased scatter is mainly due to the fact that IASI and the RS92 sensor observe different airmasses.

Figure 9 shows a profile of this IASI-RS92 differences (black line and error bars for mean differences and standard deviation of the differences, respectively). It well documents the good overall agreement between our IASI H_2O products and the Viasala RS92.

4.3 Comparison between PROFFIT-nadir and EUMETSAT level 2 products

In addition we compared to EUMETSAT level 2 H_2O products (in the following called EUM H_2O). EUMETSAT documents a vertical resolution of its level 2 H_2O profiles of

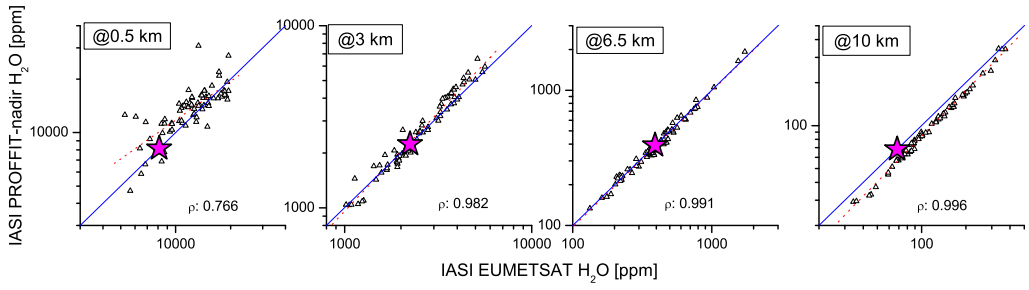

Fig. 10. Correlation plots between PROFFIT-nadir and EUMETSAT IASI H_2O data. From the left to the right for 0.5, 3, 6.5, and 10 km altitude. The magenta stars indicate the applied a priori values.

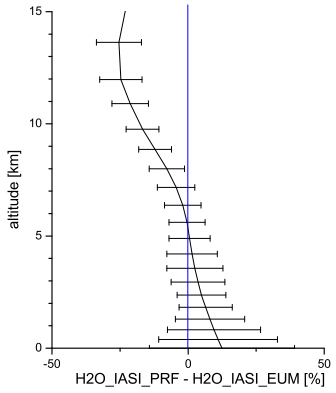

Fig. 11. Statistics of difference between PROFFIT-nadir and EUMETSAT H_2O data.

about 1–2 km (e.g., EUMETSAT IASI level 2 product guide, 2011, Figs. 4–6). This is by far better than the resolution that we obtain from our calculations. Therefore, we treat the EUM data with our averaging kernels. The so-smoothed EUM profiles should have the same characteristics than our IASI PROFFIT-nadir profiles. In order to assess the quality of the EUM data we correlate and compare them to the RS92 data. The results of this assessment are shown in the right panels of Fig. 8 and depicted as green curve in Fig. 9. The correlation coefficients are very similar to the coefficients we obtained for the correlation between PROFFIT-nadir IASI products and RS92. In both cases we observe that the correlation coefficients tend to increase from the lower to the upper troposphere, which is in agreement with lower and middle tropospheric humidity fields being more inhomogeneous than upper tropospheric humidity fields: in the lower and middle troposphere our comparison is much more affected by a mismatch in the airmass analysed by IASI, on the one hand, and by the RS92, on the other hand, than in the upper troposphere.

In the boundary layer the correlation between EUM and RS92 is slightly poorer than the correlation between the IASI PROFFIT-nadir product and the RS92. Furthermore, we observe that above 10 km the EUM concentrations overestimate the RS92 concentrations (see green curve in Fig. 9). The values of bias and scatter between EUM and RS92 data are shown in the third column of Table 4.

Figure 10 shows correlations between the IASI H_2O concentrations produced by two different retrievals: the EUMETSAT retrieval and our PROFFIT-nadir retrieval. This comparison is not affected by a potential mismatch in the airmass and above the boundary layer we observe a very large consistency between the two retrievals: correlation coefficients of larger than 0.98 and scatter smaller than 10 % (see forth column of Table 4). However, it has to be noted that our retrieval uses the EUMETSAT IASI level 2 temperature profiles as the a priori temperature, so the EUM and PROFFIT-nadir H_2O products are not fully independent.

Concerning the upper troposphere we can clearly identify a systematic wet bias of EUM with respect to PROFFIT-nadir. At 13 km this bias reaches 25 % (see Fig. 11).

In the boundary layer the correlation between the two IASI retrievals is rather poor. This suggests that the relatively poor agreement between the IASI EUM and PROFFIT-nadir H_2O, on the one hand, and the RS92 H_2O, on the other hand – as documented in the bottom panels of Fig. 8 – is not exclusively due to the aforementioned increased inhomogeneities at low altitudes. Instead, very close to the surface the IASI H_2O retrievals seem to be significantly less precise than at higher altitudes. This is exactly what is predicted by the error estimation (see Fig. 6), which indicates that close to the surface the quality of the IASI H_2O data strongly depends on the uncertainties of lower tropospheric temperatures.

4.4 Comparison to ground-based FTS

Comparing ground-based FTS data to IASI data means comparing two different remote sensing systems with different sensitivities. Some examples of typical H_2O and δD kernels obtained when analysing ground-based FTS spectra are shown in Fig. 3 of Schneider et al. (2010b). In particularly for δD the FTS and IASI kernels differ significantly.

Table 5. Relative difference between our IASI and FTS H_2O products (mean $\pm$ std of $2 \times \frac{IASI_{PRF}-FTS}{IASI_{PRF}+FTS}$) [%].

altitude region	FTS at 1100 cm^{-1}	FTS at 2700 cm^{-1}
LT (3.0 km)	-3.9 ± 23.0	-0.3 ± 22.8
MT (5.0 km)	$+3.5 \pm 25.0$	-2.4 ± 23.1
UT (9.0 km)	-4.1 ± 31.0	-14.4 ± 25.5

Furthermore, when taking the FTS data from Izaña we have to consider that the instrument measures solar absorption spectra and that it is situated at 2370 m a.s.l.: it is not sensitive to the atmosphere below 2370 m a.s.l.!

In order to support this IASI ground-based FTS comparison study we performed the FTS retrievals on the same altitude grid as the IASI retrievals and in addition applied the same a priori profiles. Therefore, the inherent scatter expected due to the different averaging kernels of the two remote sensing systems can be estimated by (Rodgers, 2000; Rodgers and Connor, 2003):

$$\mathbf{S}_{\delta \mathbf{x}} = (\mathbf{A}_{\mathrm{IASI}} - \mathbf{A}_{\mathrm{FTS}})\mathbf{S}_{\mathbf{a}}(\mathbf{A}_{\mathrm{IASI}} - \mathbf{A}_{\mathrm{FTS}})^T \quad (9)$$

Here $\mathbf{S}_{\delta \mathbf{x}}$ is a matrix containing the covariances of the inherent scatter when comparing IASI with FTS, $\mathbf{S}_{\mathbf{a}}$ is the known a priori covariance of H_2O and δD, and $\mathbf{A}_{\mathrm{IASI}}$ and $\mathbf{A}_{\mathrm{FTS}}$ are the IASI and FTS averaging kernels, respectively.

The ground-based FTS systems allow for an optimal estimation of tropospheric H_2O and δD in two different spectral regions (1090–1330 cm^{-1} and 2650–3025 cm^{-1}, Schneider et al., 2010c). Figure 12 shows the square root values of the diagonal elements of $\mathbf{S}_{\delta \mathbf{x}}$: left panel for H_2O and right panel for δD. The black solid line for the FTS retrievals at 1090–1330 cm^{-1} and the red dotted line for the FTS retrieval at 2650–3025 cm^{-1}. The blue dotted line indicates the altitude of the ground-based FTS system.

Concerning H_2O both remote sensing data are well comparable between 3 and 9 km. At higher altitudes IASI is more sensitive than the FTS system and consequently both data set are less comparable. Close to the altitude of Izaña the completely missing sensitivity of the FTS for lower tropospheric H_2O makes the two data set not comparable.

For δD the remote sensing data are best comparable at 4–5 km altitude. This is an altitude where IASI is still sufficiently sensitive and where the impact of the FTS system's missing lower tropospheric sensitivity is less important than at lower altitudes.

Figure 13 shows correlations between the IASI and the FTS H_2O concentrations for the altitudes marked in the left panel of Fig. 12 by the black thick dots and the red triangles: 3, 5, and 9 km. For both FTS retrievals the correlation coefficients are situated between 0.84 and 0.89. Table 5 collects the values of the bias and the scatter of IASI – FTS. The bias between both data sets lies generally within 5 %, except

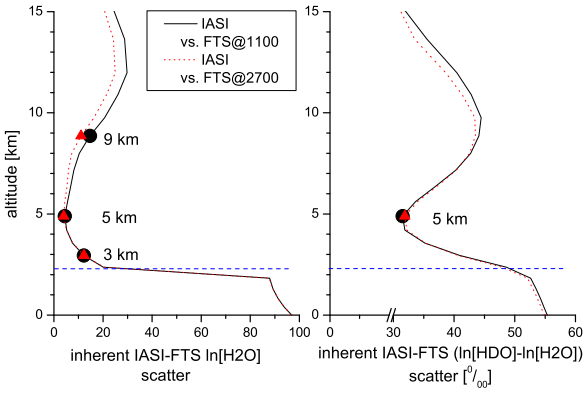

Fig. 12. Expected scatter between IASI and ground-based FTS data caused by the different sensitivity of the two remote sensing systems. Left panel for H_2O and right panel for δD.

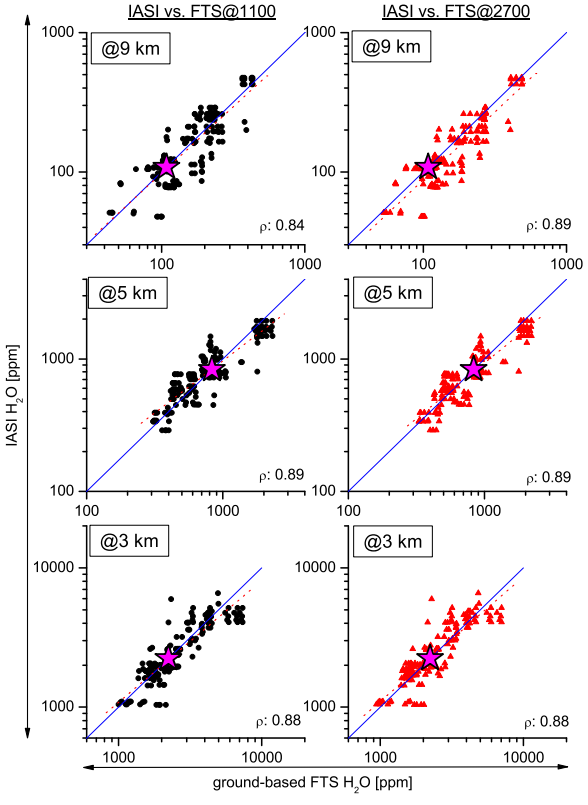

Fig. 13. Correlation plots between IASI and ground-based FTS H_2O data. From the bottom to the top for 3, 5, and 9 km altitude. Left panels for ground-based FTS retrieval 1090–1330 cm^{-1} at and right panels for ground-based FTS retrieval at 2650–3025 cm^{-1}. The magenta stars indicate the applied a priori values.

for the upper tropospheric comparison with the FTS retrieval at 2700 cm^{-1}. The good agreement confirms the results of the comparison with the RS92 H_2O data. Concerning the

scatter we find that it is mostly smaller than 30 %. This value is larger than the estimated IASI random error (see Fig. 6). Nevertheless, it is a reasonable value, since it is not only due to IASI errors. Instead it also reflects the inherent scatter when comparing IASI with FTS (see right panel of Fig. 12), the possible mismatch of the observed airmasses, and errors in the FTS data.

In Fig. 14 we compare the IASI and FTS δD values retrieved at an altitude of 5 km (where δD from IASI and the FTS system are best comparable): left panel for IASI versus FTS at 1090–1330 cm^{-1} and right panel for IASI versus FTS at 2650–3025 cm^{-1}. For both comparisons we find similar correlation coefficients of about 0.85. The slopes of the regression lines are significantly less steep than unity. This is in agreement with IASI's δD sensitivity being less than 100 % (see Fig. 3) and with the FTS's δD sensitivity being close to 100 % at this altitude (e.g., Fig. 5 of Schneider et al., 2010c).

The statistic of IASI − FTS is collected in Table 6. We observe biases that are smaller than 1 ‰! However, Fig. 14 also documents that the a priori value applied for both the IASI and the FTS retrievals lies about 25 ‰ below the red dotted linear regression line, i.e., actually there might be a small systematic difference between the IASI and the FTS δD values. The scatter of IASI − FTS is about 50 and 40 ‰. This is a large value compared to our estimated IASI δD random error of about 15 ‰. Nevertheless, there is no contradiction, since the IASI − FTS δD scatter is mainly determined by the incomparability of the two remote sensing systems. From Eq. (9) we estimate a inherent scatter of about 30 ‰ (see right panel of Fig. 12). In addition, the IASI − FTS δD scatter is affected by a possible IASI/FTS airmass mismatch and random errors of the FTS δD data.

Systematic errors in the IASI and FTS data are theoretically dominated by uncertainties in different spectroscopic line parameters. In case of the FTS data a very high accuracy of the parameters that describe the spectroscopic line shape (e.g., γ_{air} and Γ_2/Γ_0, Schneider et al., 2010c) is important. This is in contrast to the IASI data, where uncertainties in the line strength are dominating (see second panels of Figs. 4 and 5). Obviously there is no reason to expect a correlation of IASI's and FTS's systematic errors, so the small systematic differences between IASI's and the FTS's H_2O and δD as observed in this study is very encouraging.

5 Conclusions

We show that IASI thermal nadir spectra allow for an optimal estimation of middle tropospheric δD in addition to tropospheric H_2O profiles. For H_2O we estimate a very good sensitivity between the surface and the upper troposphere and a random error (dominated by atmospheric temperature uncertainties) of 35 % in the boundary layer and 15 % in the middle and upper troposphere. We estimate a sensitivity of IASI with respect to the real δD state of about 70 %. For δD errors due to temperature uncertainties widely cancel out (since errors cancel out when calculating the HDO/H_2O ratio) and the precision is controlled by measurement noise. It is about 18 ‰.

Table 6. Relative differences between our IASI and FTS δD data sets (mean $\pm$ std of $2 \times \frac{IASI_{PRF} - FTS}{IASI_{PRF} + FTS}$) [‰].

altitude region	FTS at 1100 cm^{-1}	FTS at 2700 cm^{-1}
MT (5.0 km)	$+0.9 \pm 51.7$	-0.6 ± 39.2

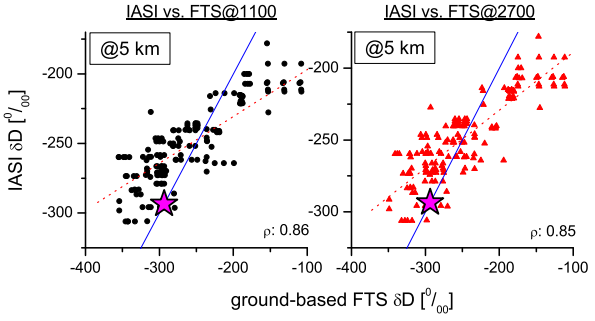

Fig. 14. Same as Fig. 13 but for δD and only for an altitude of 5 km.

Our IASI H_2O product well agrees with meteorological radiosondes and with the EUMETSAT level 2 product. The increased discrepancies close to the surface are in agreement with the theoretical estimations.

The comparison of the IASI H_2O and δD data to data obtained by a ground-based FTS system show a good consistency. Both IASI and the FTS system observe very similar lower to upper tropospheric H_2O and middle tropospheric δD values. The systematic differences between the IASI and the FTS data are rather small and will be further investigated in the near future by dedicated aircraft-based in-situ validation campaigns.

Our results indicate to the possibility of combining both remote sensing techniques. Such combination would take benefit from both the long-term characteristics of the historic ground-based FTS observations (the FTS activities date back to the 1990s at several globally distributed sites) and the wide geographical coverage of the space-based IASI observations. We plan to perform this task in the near future in the framework of the project MUSICA (MUlti-platform remote Sensing of Isotopologues for investigating the Cycle of Atmospheric water, www.imk-asf.kit.edu/english/musica).

Acknowledgements. We thank Maxim Eremenko (LISA, CNRS – Université Paris-Est Créteil, France) for his support with EUMETSAT's IASI data dissemination and formats. We acknowledge the support by the Deutsche Forschungsgemeinschaft and the Open

Access Publishing Fund of the Karlsruhe Institute of Technology. This study has been conducted in the framework of the project MUSICA which is funded by the European Research Council under the European Community's Seventh Framework Programme (FP7/2007-2013) / ERC Grant agreement number 256961.

Edited by: T. Röckmann

References

Clerbaux, C., Boynard, A., Clarisse, L., George, M., Hadji-Lazaro, J., Herbin, H., Hurtmans, D., Pommier, M., Razavi, A., Turquety, S., Wespes, C., and Coheur, P.-F.: Monitoring of atmospheric composition using the thermal infrared IASI/MetOp sounder, Atmos. Chem. Phys., 9, 6041–6054, doi:10.5194/acp-9-6041-2009, 2009.

Craig, H.: Isotopic variations in meteoric waters, Science, 133, 1702–1703, 1961a.

Craig, H.: Standard for Reporting Concentrations of Deuterium and Oxygen-18 in Natural Waters, Science, 133, 1833–1834, doi:10.1126/science.133.3467.1833, 1961b.

D'Eu, J.-F., Lemoine. B., and Rohart, F.: Infrared HCN Lineshapes as a Test of Galatry and Speed-dependent Voigt Profiles, J. Molec. Spectrosc., 212, 96–110, 2002.

Ehhalt, D. H.: Vertical profiles of HTO, HDO, and H_2O in the Troposphere, Rep. NCAR-TN/STR-100, Natl. Cent. for Atmos. Res., Boulder, Colo., 1974.

EUMETSAT IASI level 2 product guide, EUM/OPS-EPS/MAN/04/0033, www.eumetsat.int, 2011.

Frankenberg, C., Yoshimura, K., Warneke, T., Aben, I., Butz, A., Deutscher, N., Griffith, D., Hase, F., Notholt, J., Schneider, M., Schrejver, H., and Röckmann, T.: Dynamic processes governing lower-tropospheric HDO/H_2O ratios as observed from space and ground, Science, 325, 1374–1377, doi:10.1126/science.1173791, 2009.

Hase, F. and Höpfner, M.: Atmospheric raypath modelling for radiative transfer algorithms, Appl. Optics, 38, 3129–3133, 1999.

Hase, F., Hannigan, J. W., Coffey, M. T., Goldman, A., Höpfner, M., Jones, N. B., Rinsland, C. P., and Wood, S. W.: Intercomparison of retrieval codes used for the analysis of high-resolution, ground-based FTIR measurements, J. Quant. Spectrosc. Ra., 87, 25–52, 2004.

Held, I. M. and Soden, B. J.: Water Vapour Feedback and Global Warming, Annu. Rev. Energy Environ., 25, 441–475, 2000.

Herbin, H., Hurtmans, D., Clerbaux, C., Clarisse, L., and Coheur, P.-F.: $H_2^{16}O$ and HDO measurements with IASI/MetOp, Atmos. Chem. Phys., 9, 9433–9447, doi:10.5194/acp-9-9433-2009, 2009.

Joussaume, S., Jouzel, J., and Sadourny, R.: A general circulation model of water isotopes cycles in the atmosphere, Nature, 311, 24–29, 1984.

Risi, C., Noone, D., Worden, J., Frankenberg, C., Stiller, G., Kiefer, M., Funke, B. Walker, K., Bernath, P., Schneider, M., Wunch, D., Sherlock, V., Deutscher, N., Griffith, D., Wennberg, P., Strong, K., Barthlott, S., Hase, F., García, O., Smale, D., Mahieu, E., Sayres, D., Bony, S., Lee, J., Brown, D., Uemura, R., and Sturm, C.: Process-evaluation of tropospheric humidity simulated by general circulation models using water vapor isotopic observations. Part 1: comparison between models and datasets, J. Geophys. Res., submitted, 2011a.

Risi, C., Noone, D., Worden, J., Frankenberg, C., Stiller, G., Kiefer, M., Funke, B., Walker, K., Bernath, P., Schneider, M., Bony, S., Lee, J., Brown, D., and Sturm, C.: Process-evaluation of tropospheric humidity simulated by general circulation models using water vapor isotopic observations. Part 2: an isotopic diagnostic to understand the mid and upper tropospheric moist bias in the tropics and subtropics, J. Geophys. Res., submitted, 2011b.

Rodgers, C. D.: Inverse Methods for Atmospheric Sounding: Theory and Praxis, World Scientific Publishing Co., Singapore, ISBN 981-02-2740-X, 2000.

Rodgers, C. D. and Connor, B. J.: Intercomparison of remote sounding instruments, J. Geophys. Res., 108, 4116–4129, doi:10.1029/2002JD002299, 2003.

Rothman, L. S., Gordon, I. E., Barbe, A., Chris Benner, D., Bernath, P. F., Birk, M., Boudon, V., Brown, L. R., Campargue, A., Champion, J.-P., Chance, K., Coudert, L. H., Dana, V., Devi, V. M., Fally, S., Flaud, J.-M., Gamache, R. R., Goldman, A., Jacquemart, D., Kleiner, I., Lacome, N., Lafferty, W. J., Mandin, J.-Y., Massie, S. T., Mikhailenko, S. N., Miller, C. E., Moazzen-Ahmadi, N., Naumenko, O. V., Nikitin, A. V., Orphal, J., Perevalov, V. I., A. Perrin, Predoi-Cross, A., Rinsland, C. P., Rotger, M., Simecková, M., Smith, M. A. H., Sung, K., Tashkun, S. A., Tennyson, J., Toth, R. A., Vandaele, A. C., and Vander-Auwera, J.: The HITRAN 2008 molecular spectroscopic database, J. Quant. Spectrosc. Radiat. Transfer, 110, 533–572, doi:10.1016/j.jqsrt.2009.02.013, 2009.

Schneider, M., Hase, F., and Blumenstock, T.: Water vapour profiles by ground-based FTIR spectroscopy: study for an optimised retrieval and its validation, Atmos. Chem. Phys., 6, 811–830, doi:10.5194/acp-6-811-2006, 2006a.

Schneider, M., Hase, F., and Blumenstock, T.: Ground-based remote sensing of HDO/H_2O ratio profiles: introduction and validation of an innovative retrieval approach, Atmos. Chem. Phys., 6, 4705–4722, doi:10.5194/acp-6-4705-2006, 2006.

Schneider, M. and Hase, F.: Improving spectroscopic line parameters by means of atmospheric spectra: Theory and example for water vapour and solar absorption spectra, J. Quant. Spectrosc. Radiat. Transfer, 110, 1825–1839, doi:10.1016/j.jqsrt.2009.04.011, 2009a.

Schneider, M. and Hase, F.: Ground-based FTIR water vapour profile analyses, Atmos. Meas. Tech., 2, 609–619, doi:10.5194/amt-2-609-2009, 2009.

Schneider, M., Romero, P. M., Hase, F., Blumenstock, T., Cuevas, E., and Ramos, R.: Continuous quality assessment of atmospheric water vapour measurement techniques: FTIR, Cimel, MFRSR, GPS, and Vaisala RS92, Atmos. Meas. Tech., 3, 323-338, doi:10.5194/amt-3-323-2010, 2010a.

Schneider, M., Yoshimura, K., Hase, F., and Blumenstock, T.: The ground-based FTIR network's potential for investigating the atmospheric water cycle, Atmos. Chem. Phys., 10, 3427–3442,

doi:10.5194/acp-10-3427-2010, 2010b.

Schneider, M., Toon, G. C., Blavier, J.-F., Hase, F., and Leblanc, T.: H_2O and δD profiles remotely-sensed from ground in different spectral infrared regions, Atmos. Meas. Tech., 3, 1599–1613, doi:10.5194/amt-3-1599-2010, 2010c.

Schneider, M., Hase, F., Blavier, J.-F., Toon, G. C., and Leblanc, T.: An empirical study on the importance of a speed-dependent Voigt line shape model for tropospheric water vapor profile remote sensing, J. Quant. Spectrosc. Radiat. Transfer, 112, 465–474, doi:10.1016/j.jqsrt.2010.09.008, 2011.

Vömel, H., Selkirk, H., Miloshevich, L., Valverde, J., Valdés, J., Kyrö, E., Kivi, R., Stolz, W., Peng, G., and Diaz, J. A.: Radiation dry bias of the Vaisala RS92 humidity sensor, J. Atmos. Oceanic Technol., 24, 953–963, 2007.

Webster, C. R. and Heymsfield, A. J.: Water isotope ratios D/H, $^{18}O/^{16}O$, $^{17}O/^{16}O$ in and out of clouds map dehydration pathways, Science, 302, 1742–1745, 2003.

Worden, J. R., Bowman, K., Noone, D., Beer, R., Clough, S., Eldering, A., Fisher, B., Goldman, A., Gunson, M., Herman, R., Kulawik, S. S., Lampel, M., Luo, M., Osterman, G., Rinsland, C., Rodgers, C., Sander, S., Shephard, M., and Worden, H.: TES observations of the tropospheric HDO/H_2O ratio: retrieval approach and characterization, J. Geophys. Res., 111, D16309, doi:10.1029/2005JD006606, 2006.

Worden, J. R., D. Noone, K. Bowman, R. Beer, A. Eldering, B. Fisher, M. Gunson, A. Goldman, R. Herman, S. S. Kulawik, M. Lampel, G. Osterman, C. Rinsland, C. Rodgers, S. Sander, M. Shephard, C. R. Webster, and H. Worden: Importance of rain evaporation and continental convection in the tropical water cycle, Nature, 445, 528–532, doi:10.1038/nature05508, 2007.

Yoshimura, K., Kanamitsu, M., Noone, D., and Oki, T.: Historical isotope simulation using Reanalysis atmospheric data, J. Geophys. Res., 113, D19108, doi:10.1029/2008JD010074, 2008.

Yoshimura, K., C. Frankenberg, J. Lee, M. Kanamitsu, J. Worden, and T. Röckmann: Comparison of an isotopic atmospheric general circulation model with new quasi-global satellite measurements of water vapor isotopologues, J. Geophys. Res., 116, D19118, doi:10.1029/2011JD016035, 2011.

Zahn, A.: Constraints on 2-Way Transport across the Arctic Tropopause Based on O_3, Stratospheric Tracer (SF_6) Ages, and Water Vapor Isotope (D, T) Tracers, J. Atmos. Chem. 39, 303–325, 2001.